AGU PUBLICATIONS

Water Resources Research

RESEARCH ARTICLE
10.1002/2017WR021248

Key Points:
- Waves generated a wedge of elevated water content beneath the swash zone gradually expanding downward and landward
- Pore water exhibited a more rapid and deeper response to swash in high-permeability beaches
- High capillary fringe reduced swash-induced seawater infiltration but intensified the horizontal water flow driven by tides

Supporting Information:
- Supporting Information S1

Correspondence to:
M. C. Boufadel,
boufadel@gmail.com

Citation:
Geng, X., Heiss, J. W., Michael, H. A., & Boufadel, M. C. (2017). Subsurface flow and moisture dynamics in response to swash motions: Effects of beach hydraulic conductivity and capillarity. *Water Resources Research*, *53*, 10,317–10,335. https://doi.org/10.1002/2017WR021248

Received 2 JUN 2017
Accepted 20 NOV 2017
Accepted article online 27 NOV 2017
Published online 8 DEC 2017

Subsurface Flow and Moisture Dynamics in Response to Swash Motions: Effects of Beach Hydraulic Conductivity and Capillarity

Xiaolong Geng[1], James W. Heiss[2], Holly A. Michael[2], and Michel C. Boufadel[1]

[1]Department of Civil and Environmental Engineering, Center for Natural Resources Development and Protection, New Jersey Institute of Technology, Newark, NJ, USA, [2]Department of Geological Sciences, University of Delaware, Newark, DE, USA

Abstract A combined field and numerical study was conducted to investigate dynamics of subsurface flow and moisture response to waves in the swash zone of a sandy beach located on Cape Henlopen, DE. A density-dependent variably saturated flow model MARUN was used to simulate subsurface flow beneath the swash zone. Values of hydraulic conductivity (K) and characteristic pore size (α, a capillary fringe property) were varied to evaluate their effects on subsurface flow and moisture dynamics in response to swash motions in beach aquifers. The site-specific modeling results were validated against spatiotemporal measurements of moisture and pore pressure in the beach. Sensitivity analyses indicated that the hydraulic conductivity and capillary fringe thickness of the beach greatly influenced groundwater flow pathways and associated transit times in the swash zone. A higher value of K enhanced swash-induced seawater infiltration into the beach, thereby resulting in a faster expansion of a wedge of high moisture content induced by swash cycles, and a flatter water table mound beneath the swash zone. In contrast, a thicker capillary fringe retained higher moisture content near the beach surface, and thus, significantly reduced the available pore space for infiltration of seawater. This attenuated wave effects on pore water flow in the unsaturated zone of the beach. Also, a thicker capillary fringe enhanced horizontal flow driven by the larger-scale hydraulic gradient caused by tides.

1. Introduction

The swash zone, defined as that part of the beach between the wave run-down and run-up limits, has been recognized as a very dynamic region in coastal aquifer systems due to high-frequency inundation and infiltration by individual waves (Geng & Boufadel, 2017; Geng et al., 2016a; Horn, 2006; Robinson et al., 2009; Spiteri et al., 2008). Previous studies have revealed significant influences of seawater infiltration and associated mixing with groundwater on the geochemical conditions and chemical fate in nearshore beach aquifers (Jelgersma et al., 1995; Pezeshki et al., 1990; Ranjan et al., 2006; Robinson et al., 2009; Spiteri et al., 2008). Numerous studies have experimentally demonstrated the significant effects of waves on subsurface flow, especially in the saturated portion of beaches. Swash infiltration forms a water table mound beneath the swash zone that marks a groundwater divide where water flows seaward on the sea side of the mound, and landward on land side of the mound (Arnell & Reynard, 1996; Boufadel et al., 2007; Heiss et al., 2014). Meanwhile, wave motions induce an onshore upward tilt in the mean sea level, which drives groundwater recirculation from the lower end of the swash zone to the offshore wave breaking zone (Arnell & Reynard, 1996; Boufadel et al., 2007; Longuet-Higgins, 1983; Sous et al., 2013). Wave run-up and run-down on the beachface also cause high-frequency water table oscillations with a pattern similar to that induced by tides. The water table rises rapidly during the wave run-up and then falls more slowly following the wave run-down (Boufadel et al., 2007; Heiss et al., 2014; Horn et al., 1999). The high-frequency fluctuations of the water table are primarily due to two mechanisms: the pressure transmission through the saturated sediment and direct input of water through swash infiltration (Bruce, 1928; Horn, 2006; Johnson, 1967; Nielsen, 1999; Turner & Masselink, 1998).

A few field studies have been conducted to investigate the dynamics of flow and moisture movement within the unsaturated portion of the swash zone. Atherton et al. (2001) investigated temporal evolution of

water content within the uppermost portions of beach sediments in a mesotidal beach located on the southwest coast of Anglesey, north-west Wales, UK. They observed that in the upper swash zone, the water table started to rise when the run-up limit was still more than 15 m seaward of the measurement point and below the water table elevation. As the water table rise was observed to coincide with a landward movement of the water table exit point, Atherton et al. (2001) argued that the water table rising was most likely due to the horizontal movement of pore water through the capillary fringe. However, the mechanisms of pore water flow through the capillary fringe and corresponding vertical and horizontal pressure transmission have not been investigated. Heiss et al. (2014, 2015) investigated moisture dynamics beneath the swash zone and infiltration across the unsaturated beachface at two sandy beaches at Cape Henlopen, DE, USA. It was found that water content in the unsaturated region of the swash zone responded to wave run-up and swash infiltration, with a rapid rise in water content followed by a slower decline. The width of the infiltration zone was controlled by swash processes, and subaerial discharge was controlled primarily by tidal stage. These results indicated significant effects of individual waves on swash zone moisture dynamics, and consequently raised questions about how individual waves affect pore water flow pathways and associated transport processes beneath the swash zone. However, these observations were limited to two geologically similar beaches, precluding insights into how processes vary under different geologic and hydrologic conditions.

In the last two decades, numerical modeling has also been widely used to reveal swash zone dynamics. The major challenge of simulating waves and subsurface flow at the swash time scale is the high computational cost. For instance, to fully capture wave propagation and breaking along the beachface, the temporal and spatial resolutions used for Computational Fluid Dynamics (CFD) need to be on the order of milliseconds and millimeters, respectively. Therefore, two approaches were developed to upscale groundwater flow in beach aquifers under the influence of waves. Xin et al. (2010) developed a phase-averaged approach by using the mean water level as a seaward boundary condition. This approach has been used by various studies to simulate and reveal wave effects on coastal groundwater flow and solute transport processes (Robinson et al., 2014; Xin et al., 2014, 2015). Geng & Boufadel (2015c) developed a temporal upscaling approach labeled "net inflow." In that approach, spatially different infiltration rates along the beachface averaged over several wave periods were adopted as inflow boundary conditions. The modeling approach was validated against experimental data of water table elevation and tracer concentrations measured in a laboratory beach subjected to waves and tides. Although these approaches significantly improved computational efficiency, only the upscaled, or average, effects of wave swash (i.e., wave setup) on coastal groundwater systems were retained. These approaches are unable to capture moisture dynamics in the swash zone forced by wave swash.

Wave-resolving models have been developed, but they have only been applied in limited settings. Geng et al. (2014) conducted a numerical study that was based on tracer experiments in a laboratory beach conducted by Boufadel et al. (2007). Geng et al. (2014) used a phase-resolving approach to investigate the effects of waves on groundwater flow and the transport of terrestrially derived solutes in beach aquifers. The modeling results matched the water table and salt concentrations measured at numerous locations of the beach. However, in the studies of Boufadel et al. (2007) and Geng et al. (2014), the swash zone examined in the laboratory experiments was only $\sim$30 cm long, and the experiments relied on a tracer application on the beach surface to investigate the transport of dissolved nutrients in the beach due to waves. Therefore, the results do not fully represent flow and moisture dynamics in response to waves in natural beach systems, highlighting the need to implement, and test this model in field settings.

Despite the difficulty in simulation, high-frequency flow and moisture dynamics forced by wave swash are important for understanding aspects of beach aquifer systems such as subsurface geochemical conditions, particulate transport, chemical fate, surface evaporation dynamics, and aeolian sediment transport (Geng et al., 2015, 2016b; Huettel et al., 1996; Kim et al., 2017; Malott et al., 2017; Molnar et al., 2015; Nickling & Davidson-Arnott, 1990; Wu et al., 2017). Wave swash strongly controls the flux of water into beach aquifers, as well as flow paths, residence times, and mixing of various chemical species beneath the swash zone (Geng et al., 2014; Malott et al., 2016; Robinson et al., 2014; Xin et al., 2010). Moisture content is also an important control on the transport of particulates through the beach, which may be important carbon sources for biogeochemical cycling (Huettel et al., 1996; Kim et al., 2017; Malott et al., 2017). Further, variations in hydrogeological conditions such as beach aquifer permeability and capillarity also alter the wave-

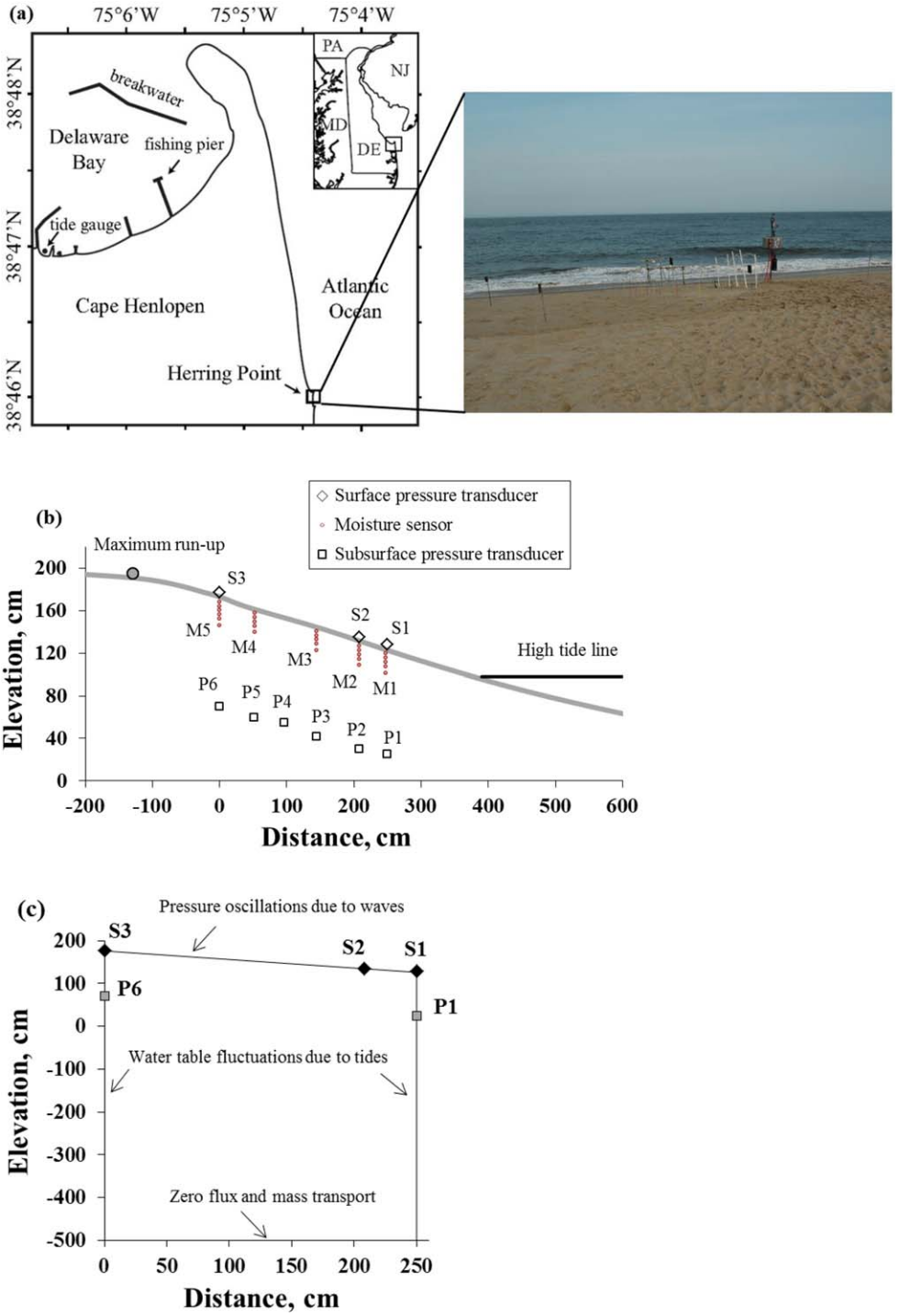

Figure 1. (a) Location of the studied beach at Herring Point, Cape Henlopen, DE (38°45′51.8″N, 75°04′54.0″W) along with a photograph showing the sampling transect; (b) cross-sectional schematic of transect instrumentation. (c) schematic of the simulated domain. Six pressure transducers (P1–P6) were installed to measure subsurface pressure change. About 25 moisture sensors were installed at five vertical (M1–M5) arrays to monitor moisture variation. Each vertical array included five moisture sensors installed at depths of 2, 6, 10, 14, and 18 cm below the beach surface, respectively. Three pressure transducers (S1–S3) were installed at the beach surface to monitor wave-induced pressure oscillation at the beachface. The elevation is relative to mean sea level (MSL). In the simulated domain, the pressure oscillations measured at S1–S3 were interpolated and used as the surface boundary condition. The pressure fluctuations measured at P6 and P1 were used as landward and seaward boundary conditions, respectively. Zero flux and mass transport were assigned at the bottom of the domain.

Table 1
Model Parameter Values Used in the Numerical Simulation

Symbol (units)	Definition	Values
α (m^{-1})	Characteristic pore-size parameter of the van Genuchten (1980) model	5.0
n	Sand grain-size distribution parameter of the van Genuchten (1980) model	7.9
K_0 (m/s)	Saturated freshwater hydraulic conductivity	2.4×10^{-4}
α_L (cm)	Longitudinal dispersivity	4.0
α_T (cm)	Transverse dispersivity	0.4
ε (Lg^{-1})	Fitting parameter of density concentration relationship	7.44×10^{-4}
S_0 (m^{-1})	Specific storage	10^{-5}
S_r	Residual soil saturation	0.10
Φ	Porosity	0.37
CONVP	The convergence criterion of pressure head in the Picard iterative scheme of MARUN code	10^{-5}
τD_m	Product of tortuosity and diffusion coefficient	10^{-9}

induced seawater infiltration and further affect the patterns of subsurface flow and moisture content in the swash zone, but the influence of these factors on swash zone moisture and flow dynamics has not been assessed.

The objectives of this paper are to (1) conduct numerical simulations supported by high-frequency field data to investigate the effects of individual swash motions on unsaturated zone pore pressure, moisture, and flow dynamics in real beach systems, and (2) test effects of various beach properties (e.g., permeability and capillarity) on processes.

The layout of the paper is as follows: First, a numerical model was used to simulate dynamics of subsurface flow and moisture response to individual waves in the swash zone of a sandy beach located on Cape Henlopen, DE. The simulation results are compared to the field data measured in Heiss et al. (2015). Then swash-induced pore pressure transmission, spatial and temporal moisture variation, subsurface flow pathways, seawater infiltration, and particle transport are quantified. Finally, a numerical sensitivity analysis is presented, across different hydraulic conductivity values and characteristic pore sizes (i.e., capillary fringe properties) to test how beach properties affect these processes.

2. Methods

2.1 Field Measurements

The field experiment was conducted on 27 June 2013 at a sandy beach located at Herring Point, Cape Henlopen, DE (Figures 1a and 1b). The intertidal zone was composed of medium sand with a median grain size of 0.39 mm. Tides were semidiurnal with a mean tidal range of 1.4 m (NOAA tidal station 8557830, Lewes, DE). Offshore significant wave height and period observed during the experiment were 0.89 m and 8.7 s (National Data Buoy Center Station 44009). A transect was deployed in the supratidal zone of the beach, which extended from 3.5 to 6.0 m landward of the high tide mark. Six instrument arrays were installed along the transect. Moisture sensors (Decagon Device EC-5) were installed in each vertical array at depths of 2, 6, 10, 14, and 18 cm below the beach surface to monitor temporal evolution of water content in response to waves (labeled as M1–M5 for each instrument array, shown in Figure 1b). A pressure transducer (Druck PTX 1835 or Druck PTX 1830) labeled as P1–P6 was placed at each array in the saturated zone to measure pore pressure. Three pressure transducers labeled as S1–S3 were placed at the sand surface to monitor swash depth along the beachface. Measurements were conducted between 5 and 16 Hz depending on the sensors for 8 h starting from the rising tide to the following ebb tide. Further details of the field measurements can be found in Heiss et al. (2015).

Table 2
Characteristics of the Numerical Experiments

Case	Hydraulic conductivity, K_0 (m/s)	Capillary fringe[a], $1/\alpha$ (cm)
1	2.4×10^{-4}	20.0
2	1.0×10^{-4}	20.0
3	5.0×10^{-4}	20.0
4	2.4×10^{-4}	5.0
5	2.4×10^{-4}	50.0

[a]The height of capillary fringe was estimated by the inverse of parameter α.

2.2. Numerical Modeling

A 2-D density-dependent variably saturated groundwater flow and solute transport model MARUN was used to simulate subsurface

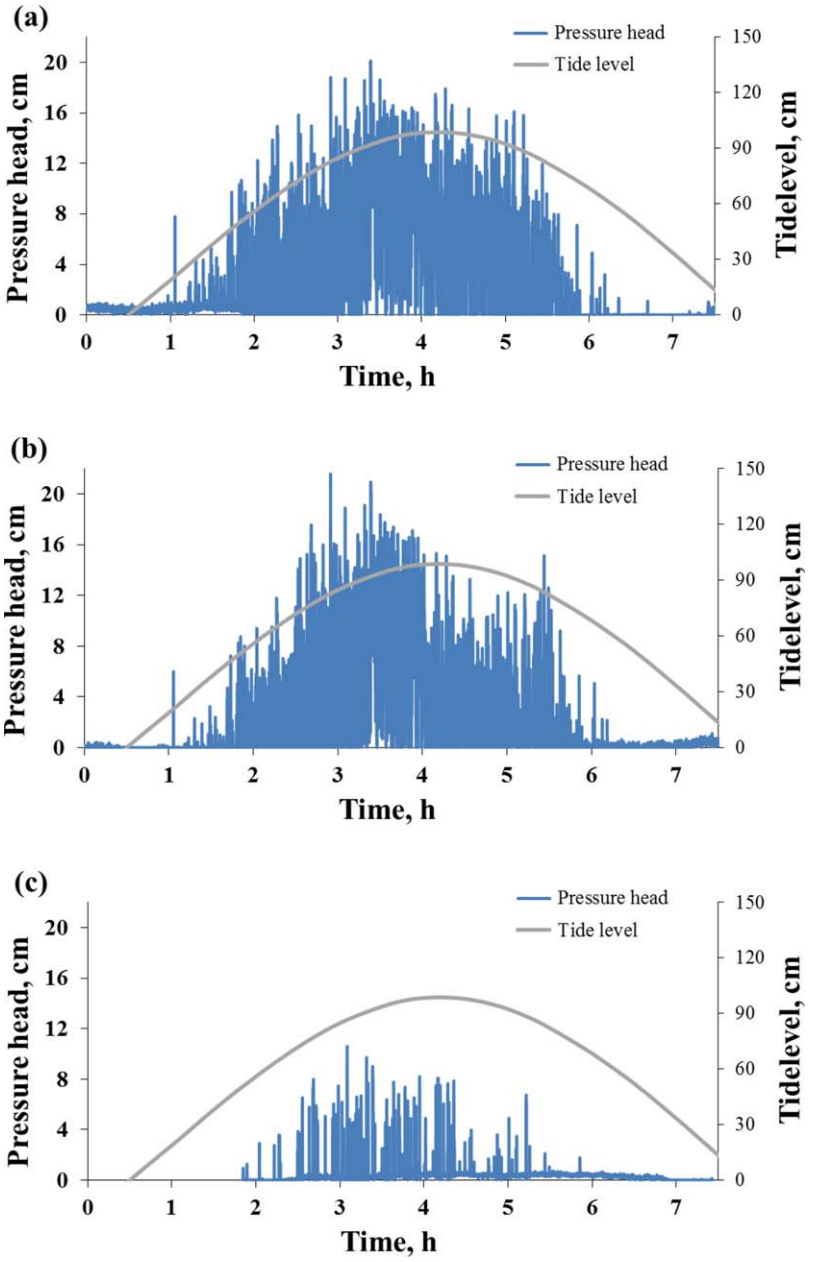

Figure 2. Swash-induced pressure oscillation measured at the beach surface by pressure transducers (a) S1, (b) S2, and (c) S3, installed at x = 245, 208, and 0.0 cm, respectively.

water flow in coastal beach aquifers subjected to waves and tides (Boufadel, 2000; Boufadel et al., 1999). The MARUN model has been validated and used extensively in our previous studies on beach hydrodynamics (Geng & Boufadel, 2015a; Geng et al., 2016b; Guo et al., 2010; Li & Boufadel, 2010). The model represented a 2-D cross-section of a beach aquifer, which was 250 cm long and 600 cm deep, and had a 17% slope (Figure 1c), spanning from the most landward instrument array to the seaward one. The domain was discretized using a mesh consisting of 50 nodes in the horizontal direction and 111 nodes in the vertical direction, resulting in a total of 5,550 nodes, and 10,780 triangular elements. The mesh resolution was ~5 cm in the horizontal direction. In vertical direction, the mesh resolution was ~2 cm above the elevation of z = 0.0 m, and ~10 cm below it. The water table observed from the most landward and seaward pressure transducers (i.e., P6 and P1, respectively) was assigned as the landward and seaward boundary conditions for flow, respectively. The pressure data recorded by the surface pressure transducers were interpolated at

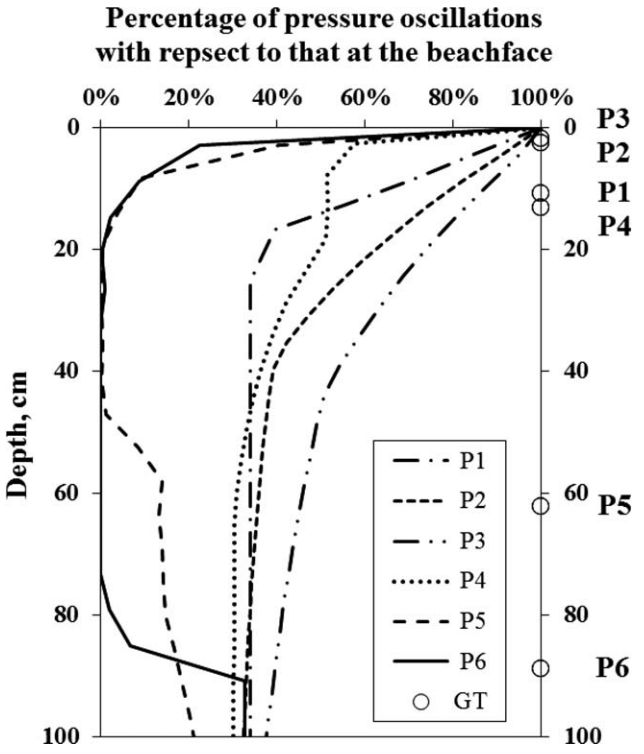

Figure 3. Vertical profiles of pressure oscillations over a wave cycle at t = 2.5 h at the horizontal locations of P1–P6. The pressure oscillations are presented as the percentage of the oscillation at the beachface. The circle symbols denote the groundwater table at each horizontal location.

each surface node and used to implement the beachface boundary: for the nodes where the interpolated pressure was more than 2 mm (i.e., the hydraulic head is greater than the elevation of the nodes by more than 2 mm), an inundated boundary condition (i.e., Dirichlet boundary condition) was assigned; otherwise, a no-flow boundary condition was assigned. A constant salinity of 5.0 g/L was assigned as the landward transport boundary condition to represent groundwater inflow. At the seaside, the model performed a check on the direction of groundwater flow across the boundary. If groundwater was flowing into the beach, a Dirichlet boundary condition was assigned with seawater concentration (35.0 g/L). If groundwater was discharging, then a Neumann boundary, $\frac{\partial c}{\partial n}=0$, was assigned, representing an outflow boundary condition where water leaves the porous domain without change in concentration.

The MARUN model was first run for approximately 10 days only with tidal forcing until hydraulic heads and concentrations reached quasi-steady state. Simulated pore pressures and salt distributions were then used as initial conditions to simulate swash-induced groundwater flow and salt transport. The time steps used for the simulations were automatically adjusted by the model to ensure that the grid Courant number was less than 1.0 ($\Delta t \leq 0.05$ s). For the base case (Case 1), the parameter values used for the simulation were summarized in Table 1. The saturated hydraulic conductivity was estimated at 2.4×10^{-4} m/s based on the grain size analysis using the Kozeny-Carman equation (Bobo et al., 2012). The height of the capillary fringe was estimated at ~20 cm based on the field observations (Heiss et al., 2015). The estimation value used in the MARUN model allowed close matching of measurements of pore pressure and moisture in the field (discussed below). In addition to the base case (Case 1, Table 2), four simulations (Cases 2–5, Table 2) were performed to examine the effects of hydraulic conductivity and beach capillarity on wave-induced water flow and moisture movement in the swash zone. Different values of hydraulic conductivity (K) and characteristic pore size (α) were adopted in the simulations. Note that the inverse of α was used to represent an estimate of the thickness of the capillary fringe, which has been widely used in our previous studies (Boufadel et al., 1998; Geng & Boufadel, 2015b; Geng et al., 2016a).

3. Results and Discussion

3.1. Temporal Evolution of Pressure and Moisture Due to Waves

Individual waves induced high-frequency pressure fluctuations at the beach surface, which led to significant vertical and horizontal pore pressure transmission beneath the swash zone. The resulting pressure gradient drove seawater into the beach and subsequently elevated the swash zone moisture content. As shown in Figure 2, waves induced significant pressure fluctuations within the swash zone surface, with high-frequency pressure fluctuations at all three sensor locations that reflect individual swash events. The amplitude of the pressure fluctuation gradually increased with time, reaching a peak between time t = 3 h and 4 h, and then gradually decreasing. The pressure fluctuations at the most landward sensor (i.e., pressure transducer S3) exhibited a smaller amplitude, lower-frequency and about a 1 h delay in comparison to those observed at the seaward sensors (i.e., pressure transducers S1 and S2). As the tide rose, the swash zone moved up the beachface, inducing the pore-pressure fluctuations at the inundated portion of the beach. During the subsequent falling tide, the fluctuations of the pressure became attenuated as swash motions gradually receded seaward. Figure 3 shows the vertical profiles of pressure oscillations over a wave cycle at t = 2.5 h at the horizontal locations of P1–P6. Note that the oscillations were presented as the percentage of the pressure oscillations at the beachface. At landward locations (e.g., P5 and P6), the pore pressure oscillations sharply damped to zero at 20 cm below the beachface. In contrast, at the same depth, the pressure oscillations were only damped to 60% and 25% at the horizontal locations of P2 and P3, respectively. The

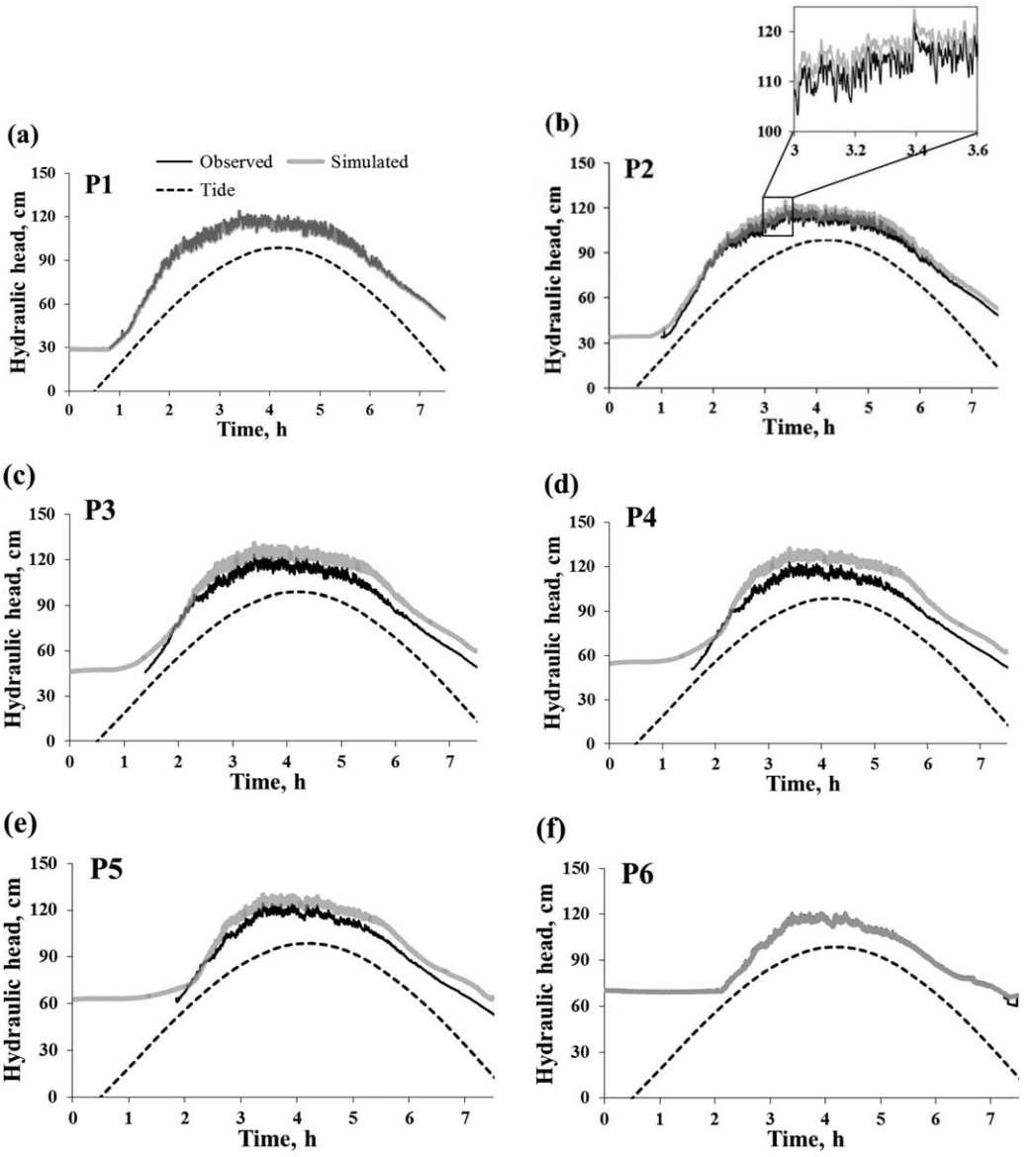

Figure 4. Observed and simulated total head at (a)–(f) pressure transducers P1–P6. Observed tide level is shown as dashed black line. Figure 4b was zoomed in to demonstrate the match of the high-frequency pressure fluctuations.

least amount pressure oscillations were shown at location P3, which is most likely due to the fact that at t = 2.5 h the water table mound was formed near the horizontal location of P3, which significantly elevated the moisture content, which attenuated pressure damping at that location. The transmission of pressure oscillations was observed through the capillary fringe, and in particular, at the horizontal locations P5 and P6, where it extended approximately 15 cm above the groundwater table. The results indicate that as wave motions acted on the beach surface, the relatively thick unsaturated zone with low moisture content significantly buffered the pressure oscillation transmitted from the beachface. Thus, the magnitude of the pressure fluctuation on the swash time scale was dependent on the moisture conditions. This phenomenon indicates that the buffering effect was more apparent at the landward side due to the thicker unsaturated zone with lower moisture content there.

Compared to tide, swash motions had negligible effects on the deeper saturated pore pressure (i.e., positive pressure). Simulated and observed hydraulic head at various locations in the beach is shown in Figures 4a–4f. The MARUN model prediction agreed well with the pressure measurements for the amplitude of fluctuations due to both waves and tides. The model slightly overestimated the absolute pore pressure measured

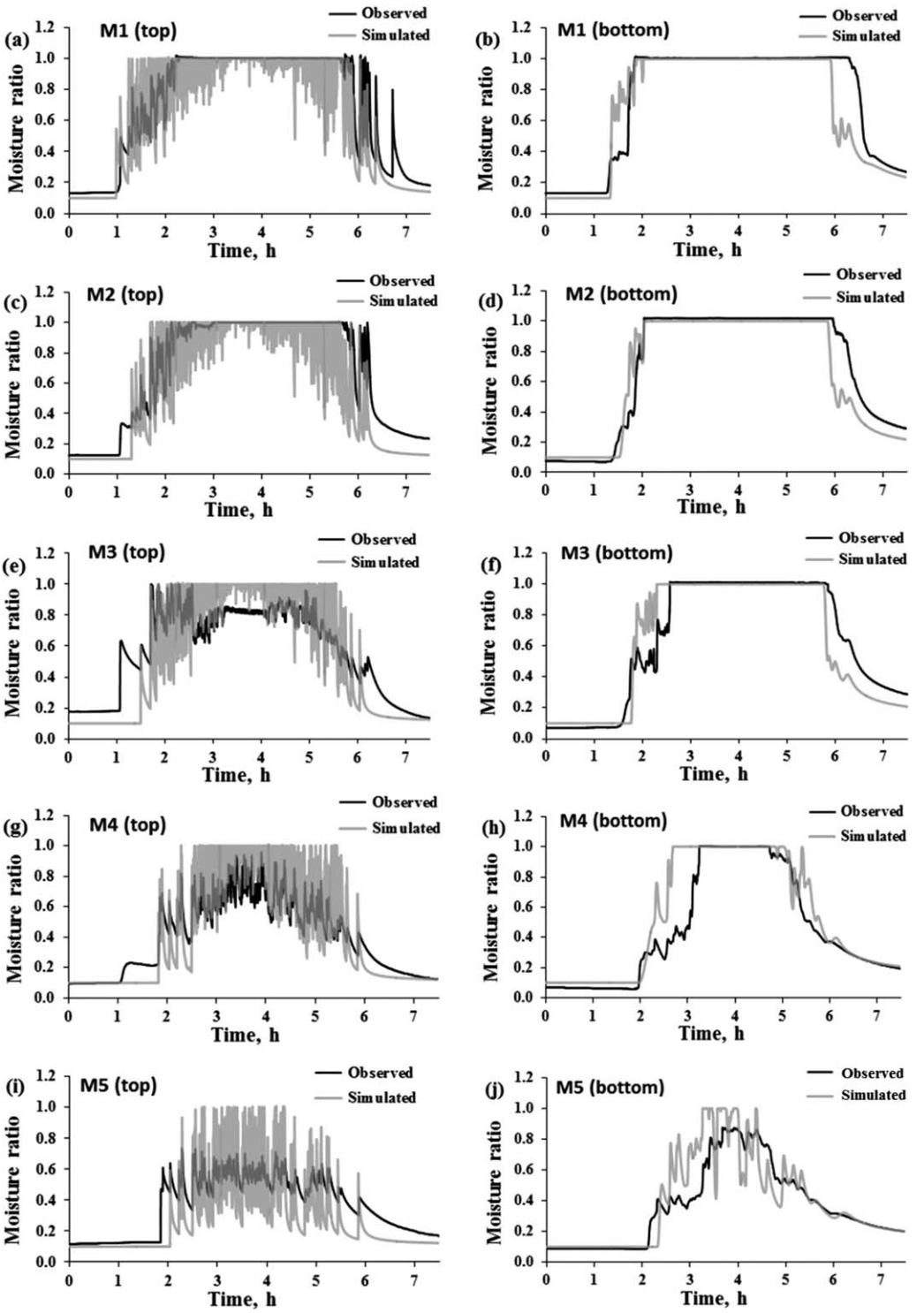

Figure 5. Observed and simulated moisture variation at top and bottom moisture sensors of each vertical array (M1–M5).

at sensors P3–P5. This was likely due to the arbitrary assumption of the landward boundary condition for the first 2 h of the simulation. A constant water table was assumed because the pore pressure could not be measured at the most landward sensor P6 in the first 2 h of the experiment, until the water table rose above the sensor. This may have caused a discrepancy between observations and simulations, especially for the

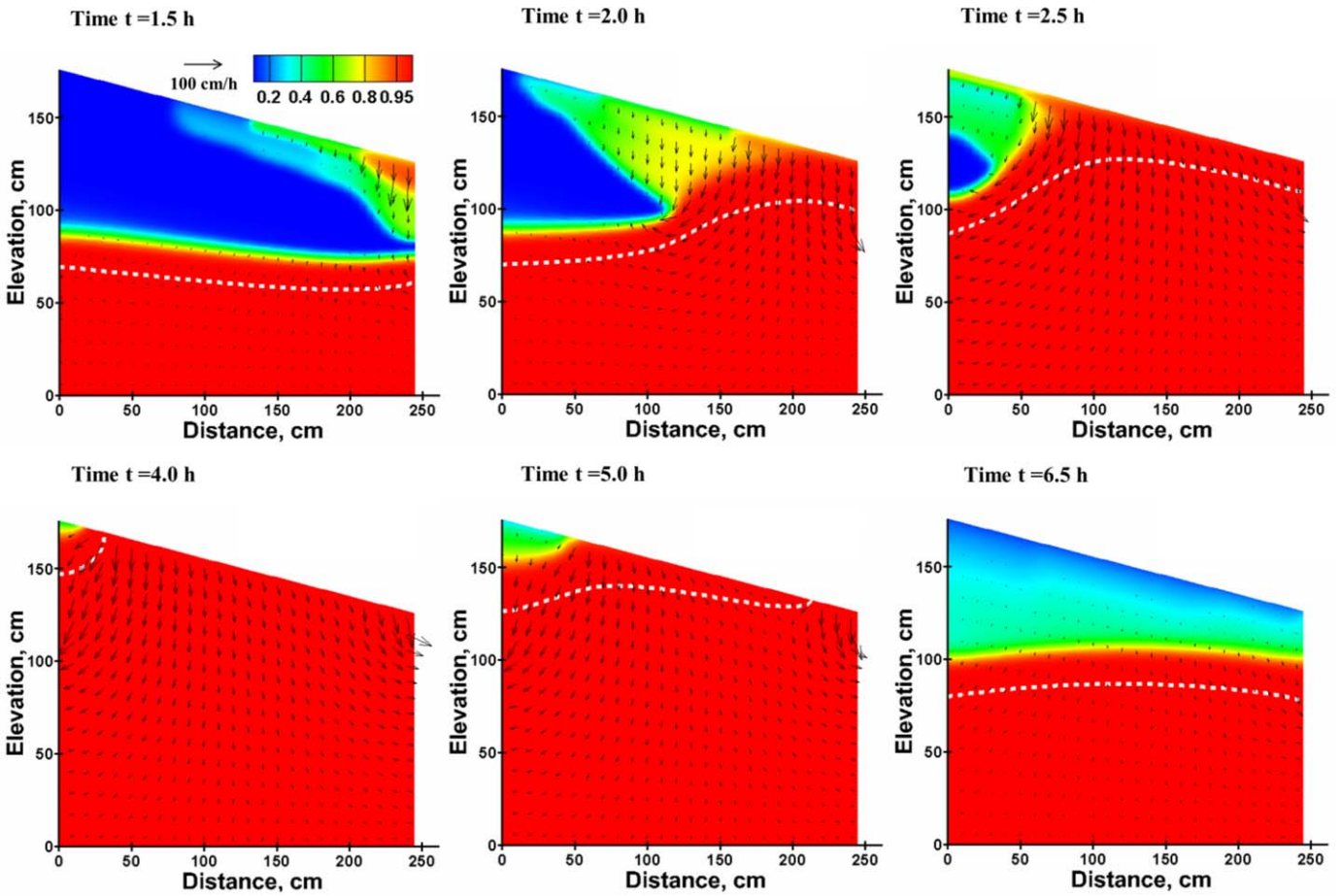

Figure 6. Simulated moisture content at different times in a tidal cycle (time t = 1.5, 2.0, 2.5, 4.0, 5.0, and 6.5 h). The white-dashed line denotes groundwater table.

sensors located close to the landward boundary (e.g., P3-–P5). The results show that pore pressure in the saturated zone responded primarily to the tide rather than to individual swash events (Figure 4). Pore pressure fluctuated typically 90 cm over the tidal cycle and only 15 cm at the swash time scale.

The moisture conditions beneath the swash zone were significantly elevated by swash motions. Observed and simulated moisture variations at the top and bottom sensors of each vertical array are shown in Figure 5. The results at the middle sensors are shown in supporting information Figure S1. For brevity, the paper discusses the moisture measured only at the top and bottom sensors of each vertical array. The numerical simulation generally captured the measured temporal evolution of moisture at all sensor locations. The mismatch between simulations and observations was in general present when the moisture content had rapid fluctuations in response to the swash motions. It is likely due to the fact that the moisture sensor measurement interval (0.2 s) was greater than the both the simulation time step (0.05 s) and the measurement interval of the surface pressure transducers (0.0625 s). Also, the equilibration time required for the moisture measurements may be somewhat greater than the measurement interval, which would result in a dampening of higher-frequency fluctuations. Therefore, it is possible that the sensors missed the moisture change occurring more rapidly than 5 Hz, which was captured by the simulations. In addition, sediment accretion of several centimeters was observed over the course of the experiments. This resulted in sensor depths which were somewhat variable with time. Because the moisture response varies strongly with depth, the mismatch could be due to an incorrect sensor depth. Supporting information Figure S2 shows the simulated moisture content 5.0 cm deeper than that of the sensors measured before the experiment started. A somewhat better match between the observations and simulations supports the possibility that the mismatch is partially due to sediment accretion. In agreement with the measurements, simulated moisture in the

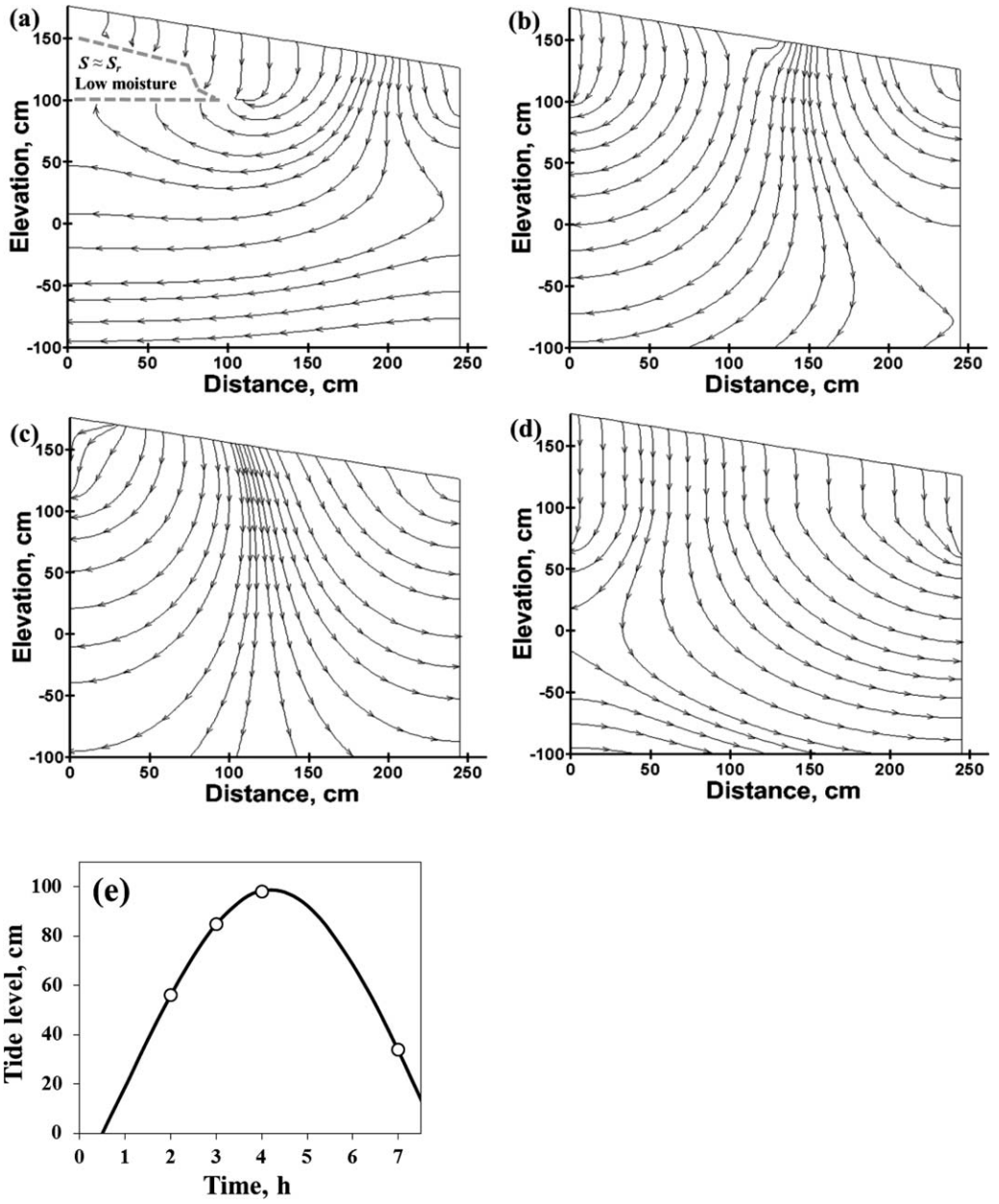

Figure 7. Simulated transient streamlines of pore water flow in the beach at time (a) t = 2.0 h, (b) t = 3.0 h, (c) t = 4.0 h, and (d) t = 7.0 h. Tidal fluctuations are provided in Figure 6e. The time points selected for the transient streamlines are marked as circle symbols in Figure 6e.

unsaturated zone of the beach significantly increased when large swash events overtopped the measurement locations, and the sediment became saturated once the swash zone moved far enough landward that swash events frequently overtopped the measurement locations. For instance, the moisture at the M1 bottom sensor increased from 0.1 to 1.0 (i.e., fully saturated) between time t = 1.5 and 2 h when large swash events started to occur on the surface. The rapid fluctuations and subsequent saturation were due to the swash-induced seawater infiltration through the beach surface. Moisture content increased first at the seaward end of the transect close to the beach surface and the area of elevated moisture content gradually expanded landward and downward. The moisture near the beach surface demonstrated high-frequency fluctuations due to individual wave run-up and run-down, which was rarely observed in the deeper unsaturated zone (e.g., at M2 top and bottom moisture sensor locations, shown in Figures 5c and 5d, respectively). Water content close to the beach surface (e.g., 2 cm below the surface) increased during wave run-up and

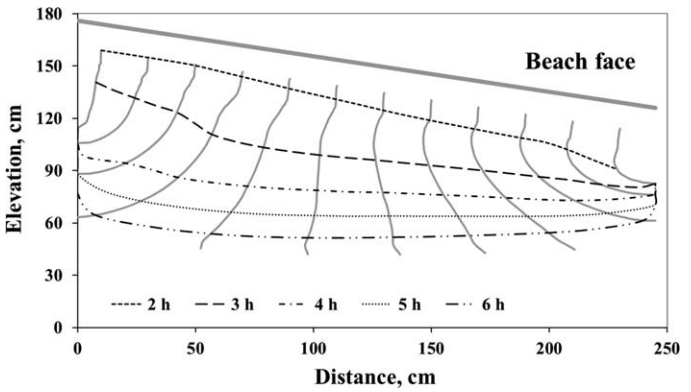

Figure 8. Simulated flow paths (grey lines) of the particles released at 10 cm below the beach surface with horizontal interval of 30 cm during the whole swash period, along with time contour lines drawn as dashed lines.

slowly declined following wave run-down. The results indicate that the response of subsurface moisture to swash motions at the beach surface was very dynamic and varied significantly over short distances. Within the unsaturated zone of the beach, swash events led to seawater infiltration, which controlled moisture conditions beneath the swash zone.

The effects of swash motions on the spatial distribution of subsurface moisture conditions were also very dynamic. Figure 6 demonstrates the simulated moisture content contours and pore water flow at various times. As expected, due to the swash infiltration, the moisture content in the shallow part of the unsaturated zone near the beach surface significantly increased (t = 1.5 h). The area of elevated moisture content gradually expanded landward and downward as swash events drove more seawater into the subsurface (t = 2.0, 2.5, 4.0, and 5.0 h), which is consistent with the moisture results measured in Heiss et al. (2014). The simulation results also indicate that the hydraulic gradient associated with the water table mound caused significant landward flow through the capillary fringe. Once the swash zone receded seaward of the instrument transect at t = 6.5 h, significant vertical drainage occurred in the unsaturated zone of the beach and the moisture content decreased. This was accompanied by horizontal saturated flow toward the sea. The results indicate that swash motions were a major driving force for water flow in the unsaturated zone of the beach.

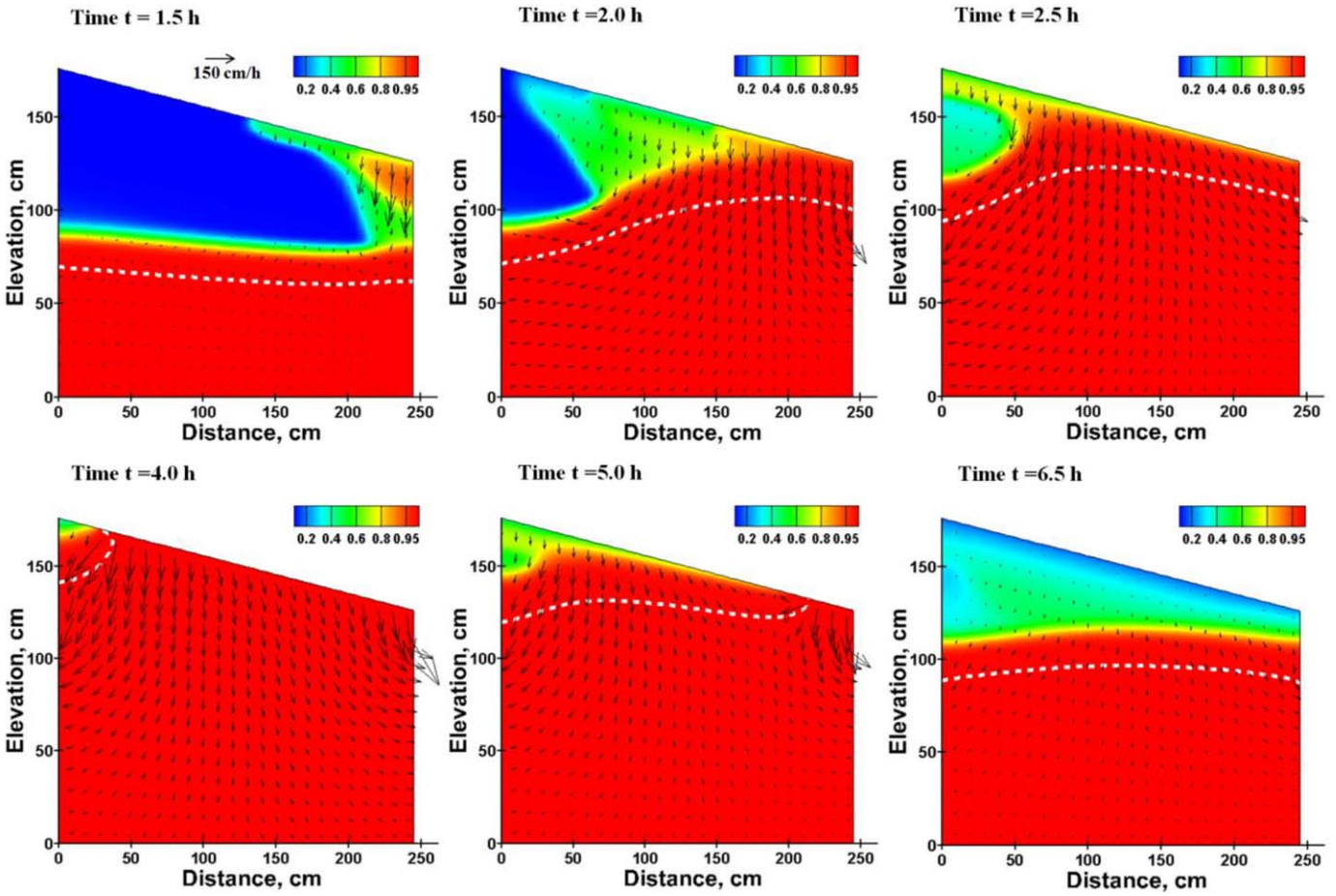

Figure 9. Simulated moisture content at different time points (time t = 1.5, 2.0, 2.5, 4.0, 5.0, and 6.5 h) for the case with $K_0 = 5.0 \times 10^{-4}$ m/s (i.e., Case 3). The white-dashed line denotes groundwater table.

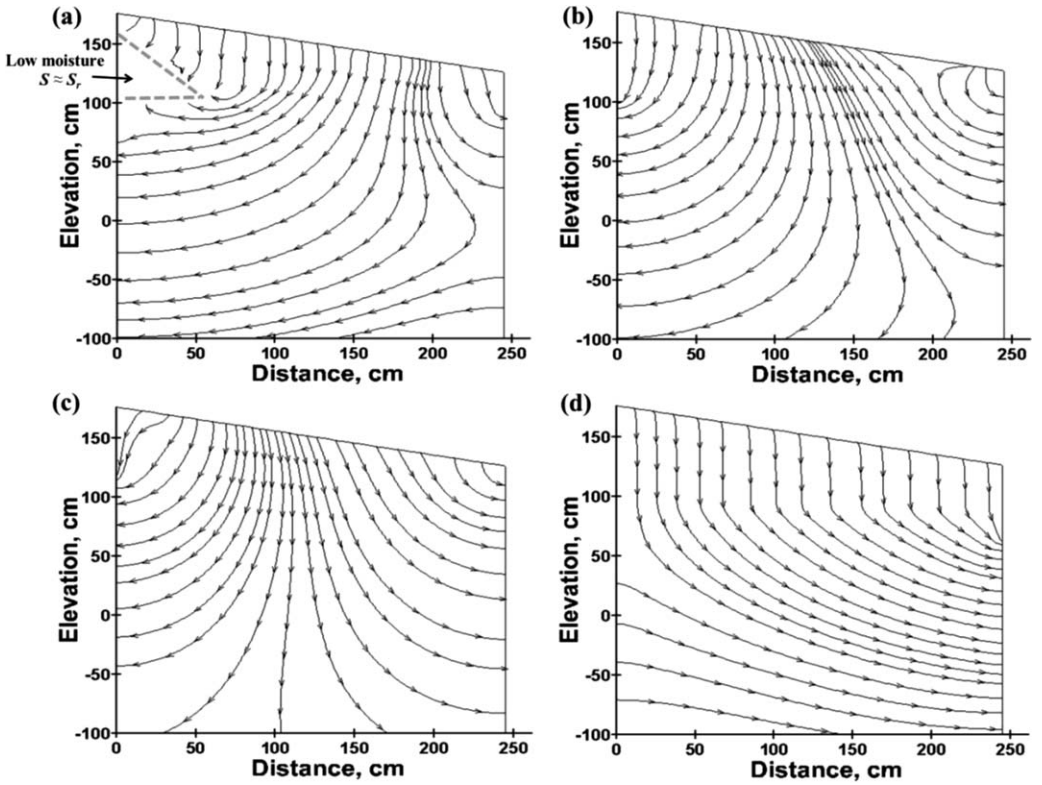

Figure 10. Simulated transient streamlines for subsurface water flow in the beach at time (a) t = 2.0 h, (b) t = 3.0 h, (c) t = 4.0 h, and (d) t = 7.0 h for the case with $K_0 = 5.0 \times 10^{-4}$ m/s (i.e., Case 3).

3.2. Subsurface Flow Dynamics Response to Waves

Swash motions altered subsurface flow patterns, generating significant vertical and horizontal pore water flow below the beachface. Figure 7 shows groundwater flow paths in the beach at various times in a tidal cycle. Note that tidal fluctuations are shown in Figure 7e. Figure 7a indicates that at time t = 2.0 h the pore water within the saturated zone of the beach flowed landward due to the rising tide. Within the upper part of the unsaturated zone, downward flow occurred due to seawater infiltration from the beachface. In the lower part of the unsaturated zone, the pore water flowed landward through the capillary fringe due to the hydraulic gradient generated by the water table mound beneath the swash zone. On the sea side of the mound, pore water flowed seaward, consistent with field measurements of Heiss et al. (2014, 2015). The model also predicted that the shallow, low-moisture portion ($S \approx S_r$) in the swash zone became wedge-shaped and gradually shrunk landward as swash motions migrated up the beach. As shown in Figure 7a, due to extremely low moisture content, pore water flow was significantly inhibited in that region. In contrast, significant flow was occurred in the swash-saturated region. This is consistent with the finding discussed above, that waves were a major driving force for the pore water to flow through the unsaturated portion of the swash zone, as the increased moisture content due to swash allowed water to move more quickly through that zone. The low-moisture zone disappeared at t = 3 h when swash-induced infiltration and tidal rise increased the water table elevation and moisture content in the whole domain (Figure 7b). Consequently, groundwater flow paths diverged as large swash events contributed seawater into the subsurface. Similar streamlines were found in the subsurface at t = 4 h (Figure 7c). Once the tide and swash zone receded seaward of the model domain at t = 7 h, pore water gradually drained from the upper beach and discharged seaward along the groundwater pathways (Figure 7d). The results indicate that the pore water flow in the unsaturated zone have a lagged response to swash. When swash motions initially appeared on the beach, the unsaturated sediment pores needed to fill (e.g., $S \gg S_r$) before water could flow markedly through the pores. Similarly, significant downward flow of residual groundwater through the unsaturated zone still occurred for drainage after the swash zone had receded seaward (Figure 7d).

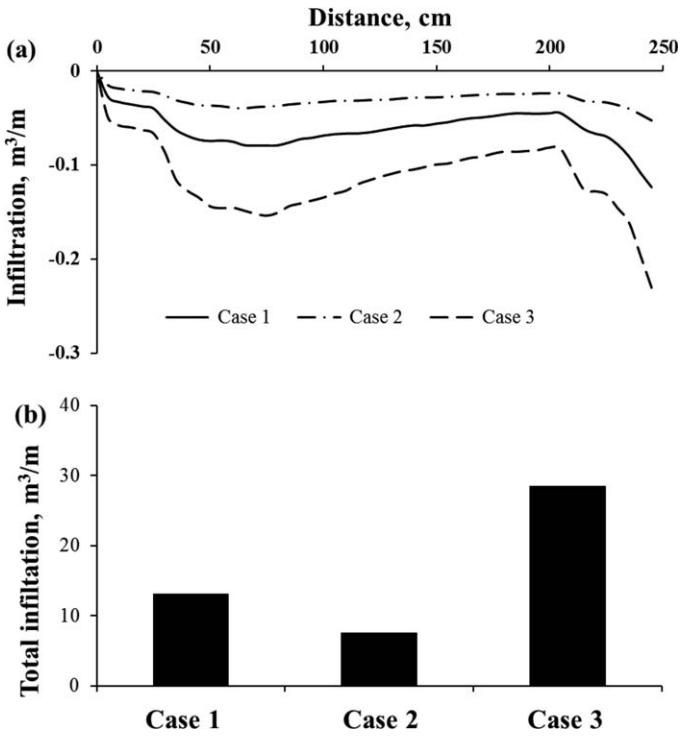

Figure 11. (a) Spatial distribution of wave-induced seawater infiltration along the beachface for the cases with different K values (i.e., Cases 1–3); (b) total seawater infiltration into the portion of the beach between $x = 0$ and 250 cm during the studied period induced by swash motions for Cases 1–3.

Particle tracking was conducted to further reveal the flow paths and associated transit times in the beach during the observed swash period, which is reported in Figure 8. The neutrally buoyant particles were released 10 cm below the beach surface at the initial time (t = 0), and the simulated transient velocity field was used for checking the particle locations at each time step. The results show that the particles released at different locations in the beach exhibited markedly different trajectories. The particles released at the landward locations between $x = 10$ cm and $x = 90$ cm migrated landward, while the particles released at the seaward locations between $x = 150$ cm and $x = 230$ cm migrated seaward. The downward motion was largest at around $x = 100$ cm. The trajectories of the released particles highlighted the divergent flow path generated by the water table mound. However, all particles initially migrated vertically once the beach surface above the particle became inundated by swash. This is consistent with the results shown in Figure 7, which demonstrate that vertical downward flow dominated in the shallow unsaturated zone. In addition, the movement of the particles was faster within the first 3 h when swash motions started to act on the beach surface. This indicates that once swash-induced seawater infiltration increased the moisture content in the shallow unsaturated zone, it generated significant downward flow. It caused the particles to migrate faster in the shallow part of the beach than in the deep saturated zone.

3.3. Effects of Hydraulic Conductivity

Beach hydraulic conductivity substantially affected both the moisture distributions and the formation of the water table mound beneath the swash zone. Cases 1–3 were simulated with different K_0 values (2.4×10^{-4}, 1.0×10^{-4}, and 5×10^{-4} m/s). The temporal evolution of moisture content at various times for Case 3 ($K_0 = 5 \times 10^{-4}$ m/s) is shown in Figure 9; Case 2 is shown in supporting information Figures S3. Compared to Case 1 ($K_0 = 2.4 \times 10^{-4}$ m/s, Figure 6), Case 4 shows that the region of higher water content in the shallow unsaturated zone expanded landward more rapidly. In particular, at t = 2.0 h, the expansion of the high moisture wedge reached the horizontal location of $x = 60$ cm, while for the base Case, it extended to $x = 120$ cm. This is because higher hydraulic conductivity induced greater infiltration, which drove more seawater to the subsurface and allowed for higher flow rates. Therefore, the swash-induced high moisture wedge would expand faster in more permeable beaches. The hydraulic conductivity also affected the water table mound. During the swash period, the mound was flatter for the cases with higher hydraulic conductivity (e.g., Case 3). This is as expected because swash-induced seawater infiltration would be redistributed more quickly in higher hydraulic conductivity beaches. Therefore, it attenuated the accumulation of the seawater infiltration beneath the swash zone and resulted in a flatter water table mound.

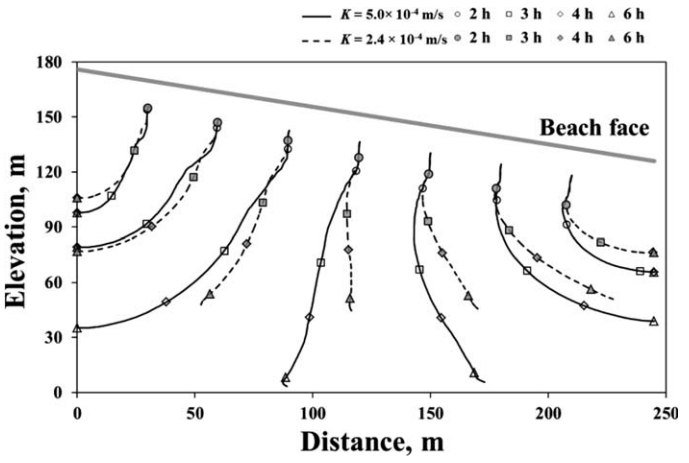

Figure 12. Simulated flow paths (grey lines) of the particles released at 10 cm below the beach surface with horizontal interval of 30 cm during the whole swash period for the cases with different values of K_0 ($K_0 = 5 \times 10^{-4}$ m/s and 2.4×10^{-4} m/s, Cases 3 and 1).

Beach hydraulic conductivity also modified subsurface flow pathways in the swash zone. Figure 10 shows the transient streamlines for Case 3 ($K_0 = 5.0 \times 10^{-4}$ m/s); Case 2 is shown in supporting information Figure S4. Compared to the Case 1 ($K_0 = 2.4 \times 10^{-4}$ m/s, Figure 7a), at t = 2.0 h, a higher hydraulic conductivity (e.g., Case 3, $K_0 = 5.0 \times 10^{-4}$ m/s) allowed the downward streamlines to extend approximately 50 cm deeper into the beach. The results indicate that swash motions had deeper impacts on subsurface flow paths in higher hydraulic conductivity beaches, which is most likely due to the higher infiltration rate. Higher hydraulic conductivity facilitated groundwater

movement through the beach and thereby helped the swash-induced seawater infiltration discharge from the beach more rapidly. At t = 7.0 h for Case 1, significant wave-induced downward movement of water could still be observed below the water table after the swash zone had moved seaward of the model domain (shown in Figure 7d). In contrast, for the high-*K* cases (e.g., Case 3), downward flow only occurred in the unsaturated zone; in the saturated zone, flow was mainly driven by the tide, indicating the swash effects almost disappeared from the model domain within 7 h.

High hydraulic conductivity significantly enhanced the seawater infiltration into the beach due to swash motions. Figure 11a shows the spatial distribution of seawater infiltration along the beach surface during the simulated period for the cases with different *K* values (i.e., Cases 1–3). As expected, with a high hydraulic conductivity value (Case 3), waves drove more seawater into the beach. In addition, for the high-*K* cases, two infiltration humps were observed at the seaward ($x = 245$ cm) and landward ($x = 60$ cm) sides of the swash zone. This is probably because the water table mound that formed in the midswash zone attenuated the seawater infiltration there, and resulted in two infiltration humps at the upper and lower portions of the swash zone. The highest infiltration rate occurred at the lower portion of the swash zone ($x = 245$ cm), which is probably because this location was exposed to waves for the longest period of time. Note that the groundwater discharge zone was farther seaward of the studied domain. Figure 11b shows the total seawater infiltration into the simulated portion of the beach during the observed period. The total infiltration over the simulation increased from 7.5 to 27.8 m^3/m when the hydraulic conductivity of the beach changed from 1×10^{-4} to 5.0×10^{-4} m/s. It indicates significant impacts of the beach hydraulic conductivity on the seawater infiltration rate induced by waves.

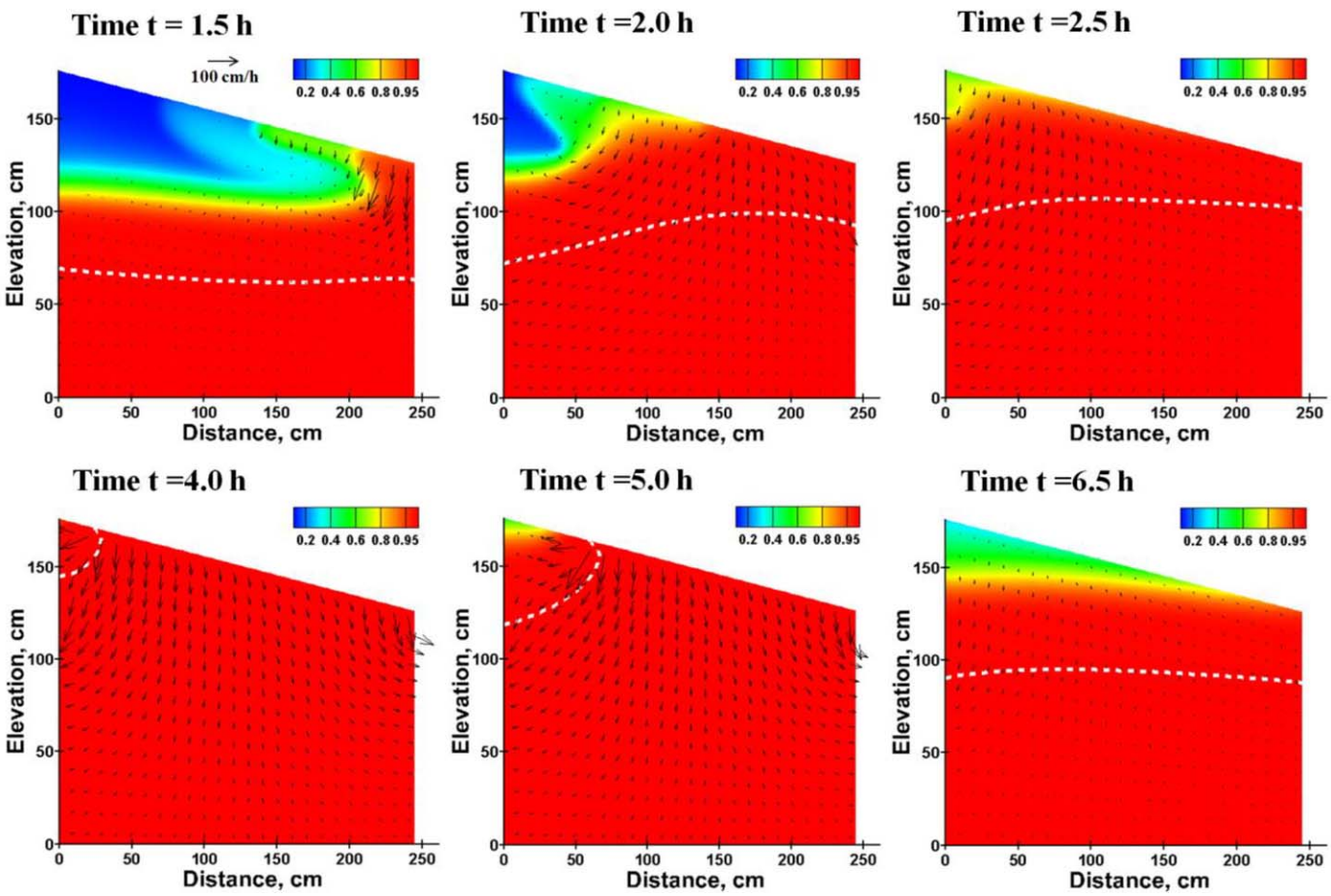

Figure 13. Simulated moisture content at different time points (time t = 1.5, 2.0, 2.5, 4.0, 5.0, and 6.5 h) for the case with capillary fringe $H_{cf} = 50$ cm (i.e., Case 5). The white-dashed line denotes groundwater table.

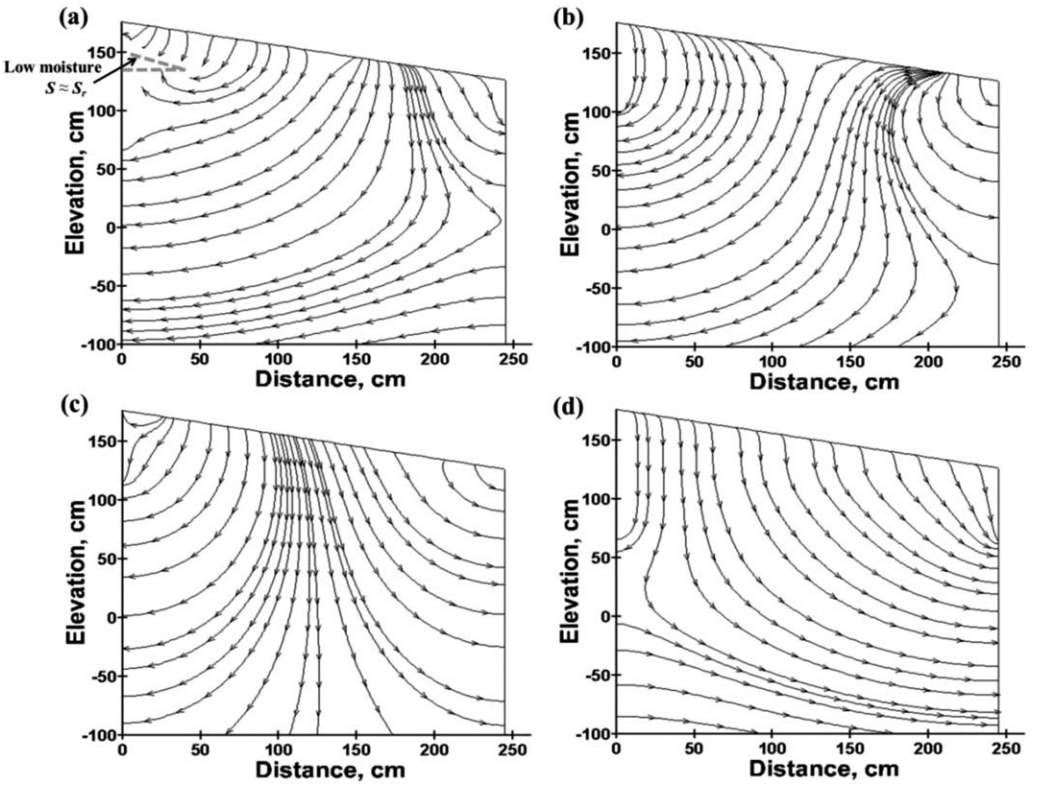

Figure 14. Simulated transient streamlines for subsurface water flow in the beach at time (a) t = 2.0 h, (b) t = 3.0 h, (c) t = 4.0 h, and (d) t = 7.0 h for the case with capillary fringe H_{cf} = 50 cm (i.e., Case 5).

The value of the saturated hydraulic conductivity also significantly affected trajectories and transit time of the particles released near the beach surface. Particle tracking was conducted for Case 3 to further evaluate the effects of hydraulic conductivity on the flow pathways and associated transit time in the beach swash zone. The simulated trajectory and transit times of the released particles for Cases 1 and 3 are shown in Figure 12. The particles released at x = 30 and 60 cm exhibited generally similar trajectories for both cases, but Case 3 had shorter transit times, which is understandable as the transit time is inversely proportional to the hydraulic conductivity. The higher hydraulic conductivity (Case 3) resulted also in different pathways for the particles; particles released at x = 90 cm migrated further landward and downward, and reached the landward boundary of the domain, in comparison to Case 1. Also, particles released at x = 120 and 150 cm migrated farther downward, and the particles released at x = 180 and 210 cm exhibited further movements in both downward and seaward directions. The major difference in the particle trajectory between Cases 1 and 3 appeared between t = 2 and 3 h, which coincided with the period that the water table mound was generated in the beach. The results indicate that high hydraulic conductivity accelerated the landward and seaward movements of the particles induced by the formation of water table mound and associated mounded capillary fringe beneath the swash zone, which significantly reduced the residence time of the particles in the swash zone.

3.4. Effects of Capillarity

A thicker capillary fringe retained higher moisture content near the beach surface. It reduced the overall moisture change beneath the swash zone and greatly diminished swash-induced infiltration. Cases 1, 4, and 5 were simulated with different characteristic pore sizes α = 0.05, 0.2, and 0.02 cm^{-1}, representing the capillary height H_{cf} = 20, 5, and 50 cm, respectively. Figure 13 shows the temporal evolution of moisture content for Case 5 (H_{cf} = 50 cm); Case 4 is shown in supporting information Figure S5. In particular, for Case 5, the low-moisture zone ($S \approx S_r$) was only observed within the top 100 cm, below which the aquifer was almost saturated. As shown in Figure 13, for Case 5, the water table mound was not clearly observed during the whole swash period. This is most likely because the greater moisture content near the beach surface

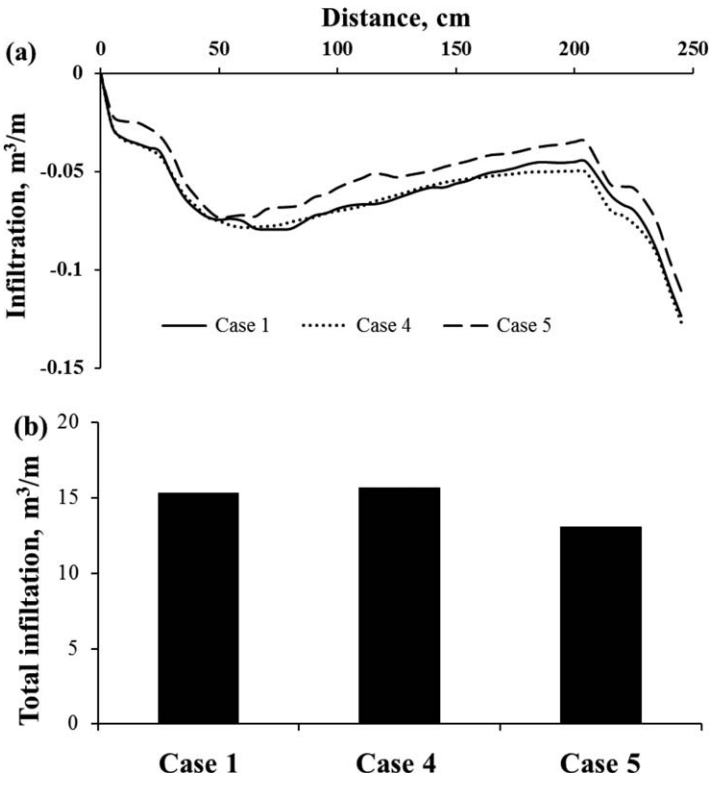

Figure 15. (a) Spatial distribution of wave-induced seawater infiltration along the beachface for the cases with different capillary fringe (i.e., Cases 1, 4, and 5); (b) Total seawater infiltration into the portion of the beach between $x = 0$ and 250 cm during the studied period induced by swash motions for Cases 1, 4, and 5.

inhibited swash-induced seawater infiltration, which reduced amount of seawater accumulating in the beach to form the water table mound.

Although a thicker capillary fringe attenuated swash effects on pore water flow in the unsaturated zone of the beach (Figure 14), it strengthened tidal effects on the supratidal zone and enhanced the movement of the pore water flow driven by a larger-scale hydraulic gradient. Figure 14 shows the simulated transient streamlines for Case 5 ($H_{cf} = 50$ cm); Case 4 is shown in supporting information Figure S6. The results show that at t = 2.0 h, with a thicker capillary fringe (e.g., Case 5), almost all the streamlines ended at the landward boundary of the domain, indicating landward horizontal flow at that time in both saturated and unsaturated zones of the beach. This is most likely due to greater moisture content in the unsaturated zone of the beach, which facilitated horizontal flow, but attenuated swash-induced vertical seawater infiltration. At t = 3.0 and 4.0 h, the streamlines were similar for the capillary cases (Cases 1, 4, and 5, Figures 7 and 14, supporting information Figure S5). Wave-induced seawater infiltration saturated the beach, and the water flow beneath the swash zone was driven downward by the swash-induced pressure oscillations at the beach surface. Note that major swash motions occurred on the surface between t = 3 and 4 h (Figure 3). Capillarity significantly affected the pore water flow even after swash receded down the beach. At t = 7.0 h, with a thicker capillary fringe, the pore water flowed more horizontally seaward through both the saturated and unsaturated zone driven by the large-scale hydraulic gradient induced by tides.

A thick capillary fringe reduced seawater infiltration induced by individual waves. Figure 15a shows spatial distribution of the seawater infiltration along the beach surface during the studied period for the H_{cf} cases (i.e., Cases 1, 4, and 5). For Case 5, with the thickest capillary fringe, waves induced the least amount of seawater infiltrating into the beach. The seawater infiltration demonstrated a similar spatial distribution along the beach surface for Cases 1 and 4 ($H_{cf} = 20$ and 5 cm, respectively). The results indicate that a thick capillary fringe retained high moisture content near the beach surface, which impeded the wave-induced seawater infiltration into the beach. In addition, as the capillary fringe became very thin (e.g., below 20 cm in this paper, Cases 1 and 4), it seemed to have negligible effects on wave-induced seawater infiltration. This is consistent with the results of the simulated total seawater infiltration induced by waves during the studied period (Figure 15b). The total volume of infiltration was 15.3, 15.6, and 13.1 m^3/m for Cases 1, 4, and 5, respectively.

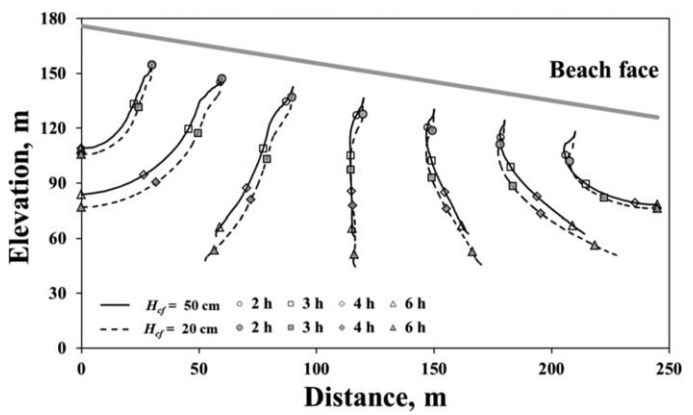

Figure 16. Simulated flow paths (grey lines) of the particles released at 10 cm below the beach surface with horizontal interval of 30 cm during the whole swash period for the cases with different values of H_{cf} ($H_{cf} = 20$ and 50 cm, Cases 1 and 5).

Capillarity impeded wave-driven unsaturated flow beneath the swash zone. It significantly altered trajectories and transit time of the particles released near the beach surface. Figure 16 shows that for Case 5, the horizontal movement of the particles was observed before waves approached the portion of the beach investigated (i.e., time t < 2 h). This is consistent with our finding (shown in Figure 14) that a thicker capillary fringe induced more-horizontal subsurface flow. The thick capillary fringe significantly impeded the movement of the particles at the swash-dominated region between $x = 50$ cm and $x = 200$ cm. During the swash cycles, due to less seawater infiltration, the particles exhibited less downward movement for Case 5, approximately 15 cm shallower than that for Case 1. Meanwhile, although a thicker capillary fringe maintained higher hydraulic conductivity in the unsaturated zone, the particles exhibited similar or less horizontal

movement for high capillary cases (e.g., Case 5), except for the first hour. This is most likely due to the fact that with larger infiltration rate, for Case 1, the particles passed through the unsaturated zone rapidly and moved into the saturated zone of the beach, while for Case 5, due to reduced seawater infiltration, the particles remained primarily in the unsaturated zone of the beach, which increased the residence time of the particles in the swash zone.

4. Conclusions

In this paper, a combined field and numerical study was performed to reveal subsurface pore water flow and moisture dynamics in response to swash on a sandy beach located at Herring Point, Cape Henlopen, DE. A density-dependent variably saturated flow model MARUN was used to simulate subsurface flow beneath the swash zone. The simulation results agreed reasonably well with the field measurements of moisture and saturated pressure. It was found that swash-induced infiltration initially filled the unsaturated pores near the beach surface, and then drove the pore water to flow farther downward. It resulted in a high moisture wedge and water table mound formed beneath the swash zone. The resulting hydraulic gradient drove the pore water to flow landward through the capillary fringe.

The saturated hydraulic conductivity and capillary fringe greatly affected swash-induced groundwater flow pathways and associated transit times. High saturated hydraulic conductivity enhanced swash-induced seawater infiltration into the beach, and resulted in a faster expansion of the high moisture wedge induced by swash cycles, and a flatter water table mound beneath the swash zone. Therefore, there was a more rapid and deep response to swash motions in the beach with higher hydraulic conductivity. Particle-tracking results indicated that high hydraulic conductivity accelerated the landward and seaward movement of water resulting from the formation of a water table mound and associated mounded capillary fringe beneath the swash zone. It significantly reduced the residence time of water in beach aquifer. In contrast, a thick capillary fringe retained higher moisture content near the beach surface, and significantly reduced the pore space available for infiltration of seawater, and therefore attenuated wave effects on pore water flow in the unsaturated zone of the beach. Conversely, the greater moisture content, strengthened the horizontal flow in the supratidal unsaturated zone of the beach, which was driven by the larger-scale hydraulic gradient as a result of tides. However, as tides had less effect on moisture variation in the supratidal zone compared to waves, a relatively thick capillary fringe diminished wave-induced seawater infiltration into the beach and reduced hydraulic exchange in the swash zone. Therefore, it increased the transit time of water beneath the swash zone.

Previous numerical investigations of aquifer dynamics caused by waves have utilized less computationally intensive phased-averaged or flow-averaged approaches in which individual wave effects on swash zone dynamics were not resolved. Our field and modeling results provide insight into the complex dynamics of subsurface pore pressure, flow, and moisture content under the influence of individual waves, which have important implications for geochemical conditions in intertidal aquifers and aeolian sediment transport. The results also reveal significant horizontal and vertical transport of the pore pressure, moisture, and water flow beneath the swash zone, and substantial effects of beach properties such as hydraulic conductivity and capillarity on aquifer-swash interactions. It highlights the need to consider individual swash motions and beach properties in studies of pore water flow, transport, and geochemistry in beach aquifers in which processes of interest are affected by high-frequency moisture and flow fluctuations.

Acknowledgments
This research paper was made possible in part by a grant from The Gulf of Mexico Research Initiative to the Consortium CARTHE II, and subsequently to the New Jersey Institute of Technology. Funding has also come from the National Oceanic and Atmospheric Administration and the Exxon Valdez Trustee Council through contract 11100836. However, no official endorsement should be implied from any of the funding entities. The data for this paper are available at http://nrdp.njit.edu/delaware_beach_wrr.

References

Arnell, N., & Reynard, N. (1996). The effects of climate change due to global warming on river flows in Great Britain. *Journal of Hydrology*, *183*(3–4), 397–424. https://doi.org/10.1016/0022-1694(95)02950-8

Atherton, R. J., Baird, A. J., & Wiggs, G. F. S. (2001). Inter-tidal dynamics of surface moisture content on a meso-tidal beach. *Journal of Coastal Research*, *17*(2), 482–489.

Bobo, A. M., Khoury, N., Li, H., & Boufadel, M. C. (2012). Groundwater flow in a tidally influenced Gravel beach in Prince William Sound, Alaska. *Journal of Hydrologic Engineering*, *17*(4), 494–494. https://doi.org/10.1061/(ASCE)HE.1943-5584.0000454

Boufadel, M. C. (2000). A mechanistic study of nonlinear solute transport in a groundwater-surface water system under steady-state and transient hydraulic conditions. *Water Resources Research*, *36*, 2549–2566. https://doi.org/10.1029/2000WR900159

Boufadel, M. C., Li, H., Suidan, M. T., & Venosa, A. D. (2007). Tracer studies in a laboratory beach subjected to waves. *Journal of Environmental Engineering*, *133*(7), 722–732. https://doi.org/10.1061/(ASCE)0733-9372(2007)133:7(722)

Boufadel, M. C., Suidan, M. T., Rauch, C. H., Venosa, A. D., & Biswas, P. (1998). 2-D variably-saturated flow: Physical scaling and Bayesian estimation. *Journal of Hydrologic Engineering*, *3*(10), 223–231. https://doi.org/10.1061/(ASCE)1084-0699(1998)3:4(223)

Boufadel, M. C., Suidan, M. T., & Venosa, A. D. (1999). A numerical model for density-and-viscosity-dependent flows in two-dimensional variably saturated porous media. *Journal of Contaminant Hydrology*, *37*(1), 1–20. https://doi.org/10.1016/S0169-7722(98)00164-8

Bruce, J. R. (1928). Physical factors on the sandy beach. Part I. Tidal, climatic, and edaphic. *Journal of the Marine Biological Association of the United Kingdom*, *15*(2), 535–552. https://doi.org/10.1017/S002531540000953X

Geng, X., & Boufadel, M. C. (2015a). Impacts of evaporation on subsurface flow and salt accumulation in a tidally influenced beach. *Water Resources Research*, *51*, 5547–5565. https://doi.org/10.1002/2015WR016886

Geng, X., & Boufadel, M. C. (2015b). Numerical modeling of water flow and salt transport in bare saline soil subjected to evaporation. *Journal of Hydrology*, *524*, 427–438. https://doi.org/10.1016/j.jhydrol.2015.02.046

Geng, X., & Boufadel, M. C. (2015c). Numerical study of solute transport in shallow beach aquifers subjected to waves and tides. *Journal of Geophysical Research: Oceans*, *120*, 1409–1428. https://doi.org/10.1002/2014JC010539

Geng, X., & Boufadel, M. C. (2017). The influence of evaporation and rainfall on supratidal groundwater dynamics and salinity structure in a sandy beach. *Water Resources Research*, *53*, 6218–6238. https://doi.org/10.1002/2016WR020344

Geng, X., Boufadel, M. C., & Cui, F. (2016a). Numerical modeling of subsurface release and fate of benzene and toluene in coastal aquifers subjected to tides. *Journal of Hydrology*, *551*, 793–803. https://doi.org/10.1016/j.jhydrol.2016.10.039

Geng, X., Boufadel, M. C., & Jackson, N. L. (2016b). Evidence of salt accumulation in beach intertidal zone due to evaporation. *Scientific Reports*, *6*, 31486. https://doi.org/10.1038/srep31486

Geng, X., Boufadel, M. C., Lee, K., Abrams, S., & Suidan, M. (2015). Biodegradation of subsurface oil in a tidally influenced sand beach: Impact of hydraulics and interaction with pore water chemistry. *Water Resources Research*, *51*, 3193–3218. https://doi.org/10.1002/2014WR016870

Geng, X., Boufadel, M. C., Xia, Y., Li, H., Zhao, L., & Jackson, N. (2014). Numerical study of wave effects on groundwater flow and solute transport in a laboratory beach. *Journal of Contaminant Hydrology*, *165*, 37–52. https://doi.org/10.1016/j.jconhyd.2014.07.001

Guo, Q., Li, H., Boufadel, M. C., & Sharifi, Y. (2010). Hydrodynamics in a gravel beach and its impact on the Exxon Valdez oil. *Journal of Geophysical Research*, *115*, C12077. https://doi.org/10.1029/2010JC006169

Heiss, J. W., Puleo, J. A., Ullman, W. J., & Michael, H. A. (2015). Coupled surface-subsurface hydrologic measurements reveal infiltration, recharge, and discharge dynamics across the swash zone of a sandy beach. *Water Resources Research*, *51*, 8834–8853. https://doi.org/10.1002/2015WR017395

Heiss, J. W., Ullman, W. J., & Michael, H. A. (2014). Swash zone moisture dynamics and unsaturated infiltration in two sandy beach aquifers. *Estuarine, Coastal and Shelf Science*, *143*, 20–31. https://doi.org/10.1016/j.ecss.2014.03.015

Horn, D. P. (2006). Measurements and modelling of beach groundwater flow in the swash-zone: A review. *Continental Shelf Research*, *26*(5), 622–652. https://doi.org/10.1016/j.csr.2006.02.001

Horn, D. P., Baldock, T. E., Baird, A. J., & Mason, T. E. (1999). Field measurements of swash induced pressures within a sandy beach. In B. L. Edge (Ed.), *Coastal engineering 1998* (pp. 2812–2825). Reston, VA: American Society of Civil Engineers.

Huettel, M., Ziebis, W., & Forster, S. (1996). Flow-induced uptake of particulate matter in permeable sediments. *Limnology and Oceanography*, *41*(2), 309–322.

Jelgersma, S., Stive, M., & Van der Valk, L. (1995). Holocene storm surge signatures in the coastal dunes of the western Netherlands. *Marine Geology*, *125*(1–2), 95–110.

Johnson, R. G. (1967). Salinity of interstitial water in a sandy beach. *Limnology and Oceanography*, *12*(1), 1–7.

Kim, K., Heiss, J., Michael, H., Cai, W.-J., Post, V., Laattoe, T., & Ullman, W. (2017). Spatial patterns of porewater reactivity in an intertidal beach aquifer. *Journal of Geophysical Research: Biogeosciences*, *122*, 2548–2562. https://doi.org/10.1002/2017JG003943

Li, H., & Boufadel, M. C. (2010). Long-term persistence of oil from the Exxon Valdez spill in two-layer beaches. *Nature Geoscience*, *3*(2), 96–99. https://doi.org/10.1038/ngeo749

Longuet-Higgins, M. S. (1983). Wave set-up, percolation and undertow in the surf zone. *Proceedings of the Royal Society of London A*, *390*(1799), 283–291.

Malott, S., O'Carroll, D. M., & Robinson, C. E. (2016). Dynamic groundwater flows and geochemistry in a sandy nearshore aquifer over a wave event. *Water Resources Research*, *52*, 5248–5264. https://doi.org/10.1002/2015WR017537

Malott, S., O'Carroll, D. M., & Robinson, C. E. (2017). Influence of instantaneous and time-averaged groundwater flows induced by waves on the fate of contaminants in a beach aquifer. *Water Resources Research*, *53*, 7987–8002. https://doi.org/10.1002/2017WR020948

Molnar, I. L., Johnson, W. P., Gerhard, J. I., Willson, C. S., & O'Carroll, D. M. (2015). Predicting colloid transport through saturated porous media: A critical review. *Water Resources Research*, *51*, 6804–6845. https://doi.org/10.1002/2015WR017318

Nickling, W. G., & Davidson-Arnott, R. G. (1990). *Aeolian sediment transport on beaches and coastal sand dunes*. Paper presented at proceedings Canadian Symposium on Coastal Sand Dunes. Coastal Zone Engineering, Institute for Mechanical Engineering, National Research Council, Ottawa, ON.

Nielsen, P. (1999). Groundwater dynamics and salinity in coastal barriers. *Journal of Coastal Research*, *15*(3), 732–740.

Pezeshki, S., DeLaune, R., & Patrick, W. (1990). Flooding and saltwater intrusion: Potential effects on survival and productivity of wetland forests along the US Gulf Coast. *Forest Ecology and Management*, *33*, 287–301.

Ranjan, P., Kazama, S., & Sawamoto, M. (2006). Effects of climate change on coastal fresh groundwater resources. *Global Environmental Change*, *16*(4), 388–399. https://doi.org/10.1016/j.gloenvcha.2006.03.006

Robinson, C., Brovelli, A., Barry, D., & Li, L. (2009). Tidal influence on BTEX biodegradation in sandy coastal aquifers. *Advances in Water Resources*, *32*(1), 16–28. https://doi.org/10.1016/j.advwatres.2008.09.008

Robinson, C., Xin, P., Li, L., & Barry, D. (2014). Groundwater flow and salt transport in a subterranean estuary driven by intensified wave conditions. *Water Resources Research*, *50*, 165–181. https://doi.org/10.1002/2013WR013813

Sous, D., Lambert, A., Vincent, R., & Michallet, H. (2013). Swash-groundwater dynamics in a sandy beach laboratory experiment. *Coastal Engineering*, *80*, 122–136. https://doi.org/10.1016/j.coastaleng.2013.05.006

Spiteri, C., Slomp, C. P., Charette, M. A., Tuncay, K., & Meile, C. (2008). Flow and nutrient dynamics in a subterranean estuary (Waquoit Bay, MA, USA): Field data and reactive transport modeling. *Geochimica et Cosmochimica Acta*, *72*(14), 3398–3412. https://doi.org/10.1016/j.gca.2008.04.027

Turner, I. L., & Masselink, G. (1998). Swash infiltration-exfiltration and sediment transport. *Journal of Geophysical Research*, *103*, 30813–30824. https://doi.org/10.1029/98JC02606

van Genuchten, M. T. (1980). A closed-form equation for predicting the hydraulic conductivity of unsaturated soils. *Soil Science Society of America Journal*, *44*(5), 892–898.

Wu, M. Z., O'Carroll, D. M., Vogel, L. J., & Robinson, C. E. (2017). Effect of low energy waves on the accumulation and transport of fecal indicator bacteria in sand and pore water at freshwater beaches. *Environmental Science & Technology*, *51*(5), 2786–2794. https://doi.org/10.1021/acs.est.6b05985

Xin, P., Robinson, C., Li, L., Barry, D. A., & Bakhtyar, R. (2010). Effects of wave forcing on a subterranean estuary. *Water Resources Research*, *46*, W12505. https://doi.org/10.1029/2010WR009632

Xin, P., Wang, S. S., Lu, C., Robinson, C., & Li, L. (2015). Nonlinear interactions of waves and tides in a subterranean estuary. *Geophysical Research Letters*, *42*, 2277–2284. https://doi.org/10.1002/2015GL063643

Xin, P., Wang, S. S., Robinson, C., Li, L., Wang, Y. G., & Barry, D. A. (2014). Memory of past random wave conditions in submarine groundwater discharge. *Geophysical Research Letters*, *41*, 2401–2410. https://doi.org/10.1002/2014GL059617